Hindawi

Research Article

Law of Countercurrent Energy Dissipation of Fresh Air by Coal and Gas Outburst Shock Waves

Haiteng Xue [1,2,3] **Xijian Li** [1,2,3] **Zhu Liu,** [1,2,3] **Fangrui Dai,** [1,2,3] **and Bei Hu** [1,2,3]

[1]*Mining College, Guizhou University, Guiyang 550025, China*
[2]*Institute of Gas Disaster Prevention and Coalbed Methane Development of Guizhou University, Guiyang 550025, China*
[3]*Engineering Center for Safe Mining Technology Under Complex Geologic Condition, Guiyang 550025, China*

Correspondence should be addressed to Xijian Li; xjli1@gzu.edu.cn

Accidental coal and gas outbursts lead to major disasters in coal-producing countries and are difficult to mitigate. To elucidate the energy dissipation law for coal and gas outburst shock waves in a complex ventilation network of mines, a coal-and-gas-outburst-energy-propagation simulation and parameter determination test device were developed and used to perform physical simulation experiments under different outburst strength conditions. These experiments were combined with numerical simulations to obtain the propagation law of outburst shock waves in a roadway and analyze different outburst intensities according to the gas counterflow criterion, highlighting the hazard characteristics of shock waves in a fresh air tunnel. The results showed that when a shock wave passed through the turning roadway, its intensity and speed were greatly attenuated and that the overpressure value of a shock wave in a straight roadway was greater than that at a corner. Upon encountering a rigid wall, the superposition of the incident and reflected shock waves increased the peak overpressure of the shock wave per unit area. When a fresh air roadway is near the coal uncovering position in rock drift ("Shimen") a corresponding counter-backflow device should be installed at the location of the connecting road near the fresh air roadway, under the condition that normal ventilation is not affected. These numerical simulation results are consistent with general experimental trends, indicating that the analyses conducted in this study are reliable and can provide a theoretical basis for the prevention of secondary disasters due to coal and gas outbursts in mines.

1. Introduction

Coal is the dominant component in China's energy mix [1, 2]. However, with the depletion of shallow coal resources and increases in energy demand, coal mining in deep mines has become a research topic [3, 4]. According to recent surveys and statistics, the deepest mining depth of coal resources in China is 2000 m and it accounts for 70% of all coal resources. Rich deep coal reserves provide China's potential energy resource [5]. However, owing to the "high ground stress, high ground temperature, and high karst water pressure" environments of deep rock masses, many mining disasters have occurred. The increased probability of mining disasters has brought huge challenges to the development of deep coal resources [6].

Coal and gas outbursts are large-scale dynamic mine phenomena that are extremely destructive and have to be characterized by complex mechanisms [6]. There are two main forms of damage [7]: first, the instantaneous ejection of high-pressured gas and coal powder. In this case, the gas flow can directly injure nearby personnel and damage the on-site structure and equipment. Second, the shock wave generated by the outburst destroys the ventilation system and causes gas backflow, which not only suffocates personnel but also causes secondary disasters such as gas and coal dust explosions. Therefore, research on coal and gas, the mechanism of gas outbursts, and the effectiveness of ventilation facilities under catastrophic conditions are important issues that must be considered for improved coal mine safety. At present, three commonly used methods explore the mechanism of coal and gas outbursts: physical simulation experiments, numerical simulations, and mathematical models. For physical simulations, experiments are based on the results of the fluid mechanics similarity criterion. According to actual conditions,

certain similarity scales may be determined for the model; thus, the results of similar simulations are more in-line with actual processes. In China, the development of a large-scale truly three-dimensional coal and gas outburst quantitative physical simulation test system, which greatly improves the similarity between the field and the simulated test conditions, breaks the traditional qualitative interpretation of coal and gas outbursts, and provides a quantitative test platform for domestic and foreign scholars to explore the mechanism of coal and gas outbursts [8]. However, with respect to coal, the high-speed and high-pressure impulse airflow generated instantaneously with a gas outburst makes it difficult to perform on-site and indoor physical simulation experiments to visually reproduce the propagation process of impingement airflow.

Numerical simulation software is usually used to analyze the distribution of impinging airflow pressure and velocity in a tunnel at different times. Li et al. [9] derived a mathematical model of unsteady airflow and gas movement based on the theory of active ventilation network, which could calculate the airflow pressure of natural gas in the ventilation system of a mine. They also verified the accuracy of the model using prominent real-world cases. The scientific formulation of emergency plans for outburst disasters provides a theoretical basis for future research. Xue et al. [10] combined the discrete-element and Boltzmann methods to construct a numerical model for coal and gas outbursts and verified the feasibility of the model using a simple two-dimensional example simulating the protrusion process. Tao et al. [11] established a coupled model for coal thermophysical properties using the theory of elasticity, seepage mechanics, and heat transfer and compared the analytical and numerical solutions to verify the model, laying a theoretical foundation for the prevention of coal and gas outbursts. However, given the complexity of the actual roadway network of mines, the numerical simulation software could not address large and complex roadway networks. Therefore, when performing numerical simulations, the employed model must also be simplified, which may easily lead to a deviation of the results. In addition, in terms of mathematical models, mathematical analysis methods are mainly used to predict the risk of coal and gas outbursts [12–16] and do not employ a complete mechanical model. The above-mentioned research has provided an improved understanding of coal and gas outbursts. However, these different methods still present drawbacks due to insufficient understanding of the coal and gas outburst mechanism to be used in the field for forecasting, resulting in the continued occurrence of coal and gas outburst accidents. This indicates that in addition to studying the coal and gas outburst mechanism, coal and gas outbursts and the laws governing the movement of shock waves in complex roadways must also be further explored.

Elucidating the propagation of shock waves in mine tunnels after coal and gas outbursts is the key to reducing outbursts that cause secondary disaster accidents. Zhou et al. [17, 18] analyzed the formation and propagation process of the coal–gas two-phase flow in different types of tunnels and found that shock waves had the best attenuation effect in a T-shaped roadway. Wang et al. [19] combined numerical simulations and experiments to study prominent shock wave and gas flow characteristics and found that when the shock wave and airflow

propagated toward the intersection, turbulence, reflection, and diffraction phenomena would occur. Furthermore, for most of them, the shock wave and airflow propagated to the roadway on the opposite side of the intersection. However, the afore-mentioned study did not involve interactions between the overpressure of shock waves and mine ventilation resistance after outbursts of coal and gas. Moreover, few studies have been conducted on the hazard characteristics of an outburst shock wave in a fresh air tunnel when the outburst of coal and gas occurs, and the outburst-prevention door is intact.

In view of this, this study describes a self-developed "coal and gas outburst energy propagation simulation and pa-rameter determination test device," which was combined with numerical simulation methods to study both the propagation of outburst shock waves in a complex venti-lation network and differences according to the gas coun-terflow criterion. Under the condition of outburst strength, the outburst shock wave presents the characteristics of gas counterflow in a fresh air tunnel. This study is expected to provide theoretical support for the prevention of secondary disasters related to coal and gas outbursts and emergency rescue.

2. Materials and Methods

2.1. Prominent Shock Wave Propagation Governing Equation. The continuity, momentum, energy, and composition equations of gases are used to describe the dynamic process of prominent shock wave propagation. The governing equation for prominent shockwave propagations are as follows:

$$
\begin{cases}
\dfrac{\partial \rho}{\partial t} + \dfrac{\partial (\rho \mu_i)}{\partial x_i} = 0, \\[2ex]
\dfrac{\partial (\rho \mu_i)}{\partial t} + \dfrac{\partial (\rho \mu_j \mu_i)}{\partial x_j} = -\dfrac{\partial p}{\partial x_i} + \dfrac{\partial \tau_{ij}}{\partial c_j} + \rho g_i + F_i, \\[2ex]
\dfrac{\partial (\rho E)}{\partial t} + \dfrac{\partial (\mu_i (\rho E + p))}{\partial x_i} \\[2ex]
= \dfrac{\partial}{\partial x_i}\left(k_{eff}\dfrac{\partial T}{\partial x_i} - \sum_{j'} h_{j'} J_{j'} + \mu_i (\tau_{ij})_{eff} + S_h\right), \\[2ex]
\dfrac{\partial (\rho \mu Y_i)}{\partial t} + \nabla \cdot (\rho \overrightarrow{v} Y_i) = -\nabla \cdot \overrightarrow{J}_i + R_i + S_i, \\[2ex]
\overrightarrow{J}_i = -\rho D_{i,m}\nabla Y_i,
\end{cases}
\tag{1}
$$

where τ_{ij} is the stress tensor, ρ is the gas density, S_i is the discrete term, F_i is the volumetric stress, ρ_{gi} is the gravi-tational volume force, $J_{j'}$ is the diffusion flux, and R_i is the netsource term for the chemical reaction.

The flow of coal and gas outburst shock waves is tur-bulent; therefore, the effect of turbulence needs to be con-sidered in the simulation. The $k-\varepsilon$ turbulence model can be expressed as follows:

$$\begin{cases} \rho \dfrac{Dk}{Dt} = \dfrac{\partial}{\partial x_i}\left[\left(\mu + \dfrac{\mu_t}{\mu_k}\right)\dfrac{\partial k}{\partial x_i}\right] + G_k + G_b - \rho\varepsilon - Y_M, \\ \\ \rho \dfrac{D\varepsilon}{Dt} = \dfrac{\partial}{\partial x_i}\left[\left(\mu + \dfrac{\mu_t}{\mu_k}\right)\dfrac{\partial \varepsilon}{\partial x_i}\right] + C_{1z}\dfrac{\varepsilon}{k}(G_k + C_{3z}G_b) - C_{2z}\rho\dfrac{\varepsilon^2}{k}, \end{cases} \quad (2)$$

where Y_M is the contribution of the compressible turbulent pulsation expansion, G_b is the turbulent energy produced by buoyancy, and G_k is the turbulent energy produced by the average velocity gradient. Here, $C_{1z} = 1.44$, $C_{2z} = 1.92$, and $C_\mu = 0.09$.

2.2. Numerical Model.

Owing to the complexity of the physical test roadway network, the numerical simulation software could not achieve convergence. Therefore, according to the focus of the research, the test roadway was simplified, and a two-dimensional model for the prominent shock wave was subsequently established, as shown in Figure 1. This model mainly consists of the prominent cavity and ventilation network of the roadway in two parts. The size of the protruding cavity is $50\,\text{cm} \times 30\,\text{cm} \times 30\,\text{cm}$, and the size of the simulated roadway is $20\,\text{cm} \times 20\,\text{cm}$. The initial conditions used in this study are presented in Table 1.

2.3. Experimental Design of the Shock Wave Test System.

To verify the results of the numerical simulations, a new coal and gas outburst energy propagation simulation and parameter determination test device is presented. The test system is based on a complex ventilation network and is designed to be scaled down. The system mainly consists of outburst cavities, simulated mine tunnels, pressure sensors, and ventilation power. A system and data acquisition terminal system are also included. A schematic of the test system is shown in Figure 2 with arrows indicating the flow direction of fresh airflow, and the straight roadway, where measurement points 4 and 5 are located, is the fresh air roadway. The size of the experimental roadway is $20\,\text{cm} \times 20\,\text{cm}$.

After vacuumizing the protruding chamber for 1 h, open the valve connected to the high-pressure tube of the gas cylinder to fill the protruding chamber with nitrogen. The charging pressure is 0.3, 0.4, 0.5, 0.7, 0.9, and 1 MPa, and the step charging is carried out with 0.1 MPa as a step until the pressure reaches the set value and becomes stable. Close the high pressure pipe valve connected to the gas cylinder, stand still for 30 s, and move the quick pressure relief device manually to simulate the start of protruding.

2.4. Gas Counterflow Model.

Gas counterflow is the main factor behind a large number of underground worker deaths. There are two forms of counterflow: one in which an instantaneously high concentration of gas directly causes suffocation and death of on-site staff; the other in which a high concentration of gas reverses the ventilation airflow and causes a large amount of highly poisonous gases. Harmful gas enters the fresh air tunnel, causing workers outside the door and other workplace personnel to suffocate and die.
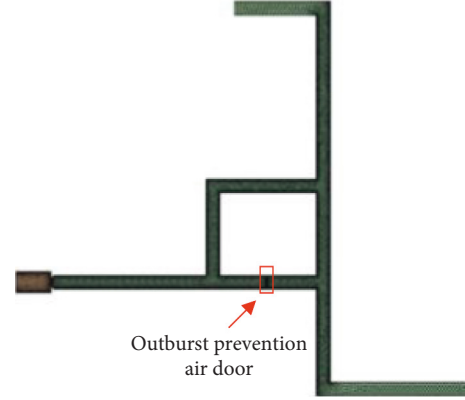

FIGURE 1: Meshing of the geometric model.

TABLE 1: Model initialization parameter settings.

	Parameter	Initial value	Unit
In the lane	Gas type	Air	
	Gas flow rate	0	m³/s
	Proportion of gas volume	0	m³/m³
	Gas temperature	300	K
	Gas pressure	0.1	MPa
Inside the cavity	Gas type	CH_4	
	Proportion of gas volume	1	m³/m³
	Gas temperature	300	K
	Gas pressure	1, 0.9, 0.7, 0.5, 0.4	MPa

When the overpressure of the protruding shock wave is greater than the ventilation resistance of a certain section of the mine, it causes the airflow in that section of the tunnel to reverse, leading to gas reversal. In the calculations, the following assumptions are made:

(1) The simulated roadway in the physical test is a horizontal roadway with no height differences

(2) The gas flow after protrusion is comprised of an incompressible gas

(3) The changes in the temperature are ignored

The only possible situation in which the gas can reverse its direction after an outburst is when the total energy of the outburst shock wave is greater than the ventilation resistance of the tunnel. The theoretical condition for this is [20] as follows:

$$P_2 - P_0 + \left(\frac{\mu_2^2}{2} - \frac{\mu_0^2}{2}\right)\rho + g\rho(Z_1 - Z_0) > h_R, \quad (3)$$

where ρ is the air density (kg/m³); g is the acceleration due to gravity (m/s²); Z_1 and Z_2 are the elevations from the reference plane, m; h_R is the ventilation resistance, N/m²–this is a pressure unit, not resistance; μ_2 is the shock wave front velocity, m/s; μ_0 is the airflow velocity under ventilation conditions, m/s; P_0 is the atmospheric pressure, which is 101.325 kPa; and P_2 is the shock wave pressure, kPa.
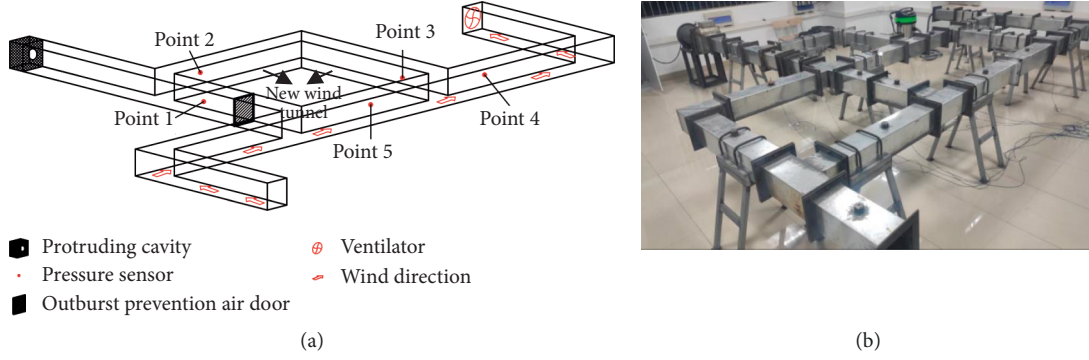
FIGURE 2: Physical experimental system. (a) Schematic of the physical experiment system. (b) Experimental system diagram.

The shock wave front velocity μ_2 may be expressed as [21] follows:

$$u_2 = c_1 \sqrt{1 + \frac{k+1}{2k} \frac{P_2}{P_0}}, \tag{4}$$

where c_1 is the speed of sound (340 m/s).

Ventilation resistance is the sum of the frictional and local resistances, which may be described as follows:

$$h_R = h_f + h_P$$
$$= \frac{\alpha L U Q^2}{S_1^3} + \xi \frac{\rho Q^2}{2 S_1^2}, \tag{5}$$

where h_f is the frictional resistance (N/m^2), h_P is the local resistance (N/m^2), α is the frictional resistance coefficient (kg/m^3); L is the length of the roadway (m), U is the perimeter of the roadway section (m), Q is the local section air volume (m^3/min), and ξ is the dimensionless local resistance coefficient.

After an outburst, a shock wave cannot continue to propagate in the roadway, and thus, there is no gas backflow, that is, the protruding shock wave does not generate frictional resistance against the wall of the roadway. Therefore, only local resistance in the roadway is considered, and equation (5) may be described as follows:

$$h_R = h_p$$
$$= \xi \frac{\rho Q^2}{2 S_1^2}. \tag{6}$$

The local resistance coefficient can be expressed as follows:

$$\xi == \left(1 - \frac{S_0}{S_1}\right)^2. \tag{7}$$

Substituting equation (6) into equation (3), the results can be denoted as follows:

$$P_2 - P_0 + \left(\frac{\mu_2^2}{2} - \frac{\mu_0^2}{2}\right)\rho + g\rho(Z_1 - Z_0) > \xi \frac{\rho Q^2}{2 S_1^2}. \tag{8}$$

TABLE 2: Model parameters.

Parameter	Value	Unit
A	0.0086	N s^2/m^4
U	0.80	m
Q	3.60	m^3/min
S_1	0.04	m^2
P	1.29	Kg/m^3
μ_0	1.50	m/s

The roadway is horizontal and straight, with no differences in height; thus, equation (8) may be expressed as follows:

$$P_2 - P_0 + \left(\frac{\mu_2^2}{2} - \frac{\mu_0^2}{2}\right)\rho > \xi \frac{\rho Q^2}{2 S_1^2}. \tag{9}$$

Based on equation (9), the gas counterflow criterion may be obtained as follows:

$$P_2 > \xi \frac{\rho Q^2}{2 S_1^2} + P_0 - \left(\frac{\mu_2^2}{2} - \frac{\mu_0^2}{2}\right)\rho. \tag{10}$$

Substituting equations (4) and (7) into equation (10), we obtain the following equation:

$$P_2 > \left(1 - \frac{S_0}{S_1}\right)^2 \frac{\rho Q^2}{2 S_1^2} + P_0 - \left(c_1^2 \frac{2k P_0 + P_2(k+1)}{4k P_0} - \frac{\mu_0^2}{2}\right)\rho. \tag{11}$$

Let $\Delta P = (1 - S_0/S_1)^2 \rho Q^2/2 S_1^2 + P_0 - (c_1^2 2k P_0 + P_2(k+1)/4k P_0 - \mu_0^2/2)\rho$. Equation (11) may then be expressed as follows:

$$P_2 > \Delta P. \tag{12}$$

By substituting the parameters and test data in Table 2 into (11), ΔP is obtained and compared to P_2. When $P_2 > \Delta P$, gas backflow occurs.

3. Results and Discussion

3.1. Simulation Result. Figure 3 shows simulation results for the cloud diagram of the pressure and velocity changes of the protruding shock wave when the protruding pressure is 1 MPa and $t = 3$–10 ms.
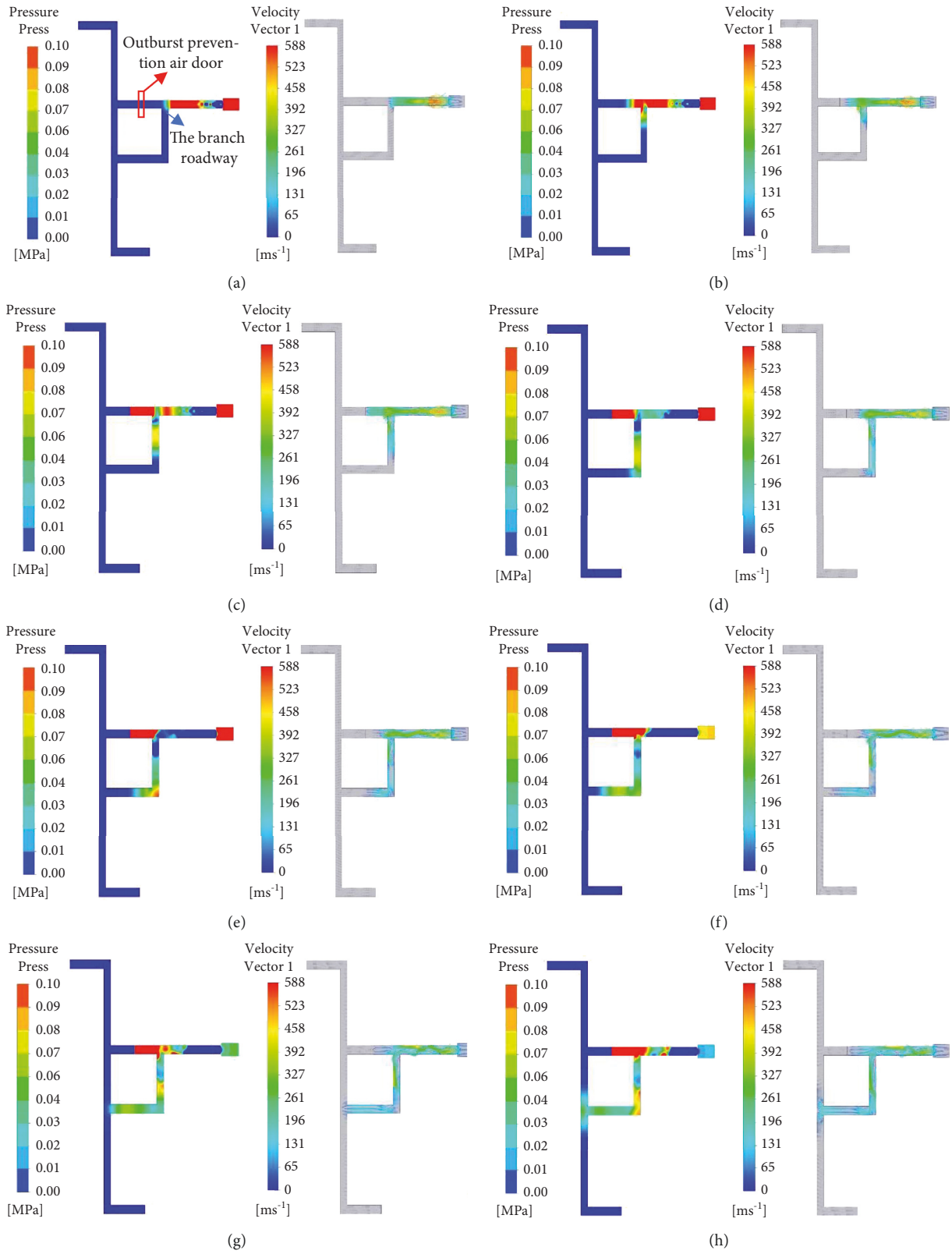
FIGURE 3: Cloud diagram of pressure and velocity changes in the prominent shock wave at different times. (a) $t = 3$ ms. (b) $t = 4$ ms. (c) $t = 5$ ms. (d) $t = 6$ ms. (e) $t = 7$ ms. (f) $t = 8$ ms. (g) $t = 9$ ms. (h) $t = 10$ ms.
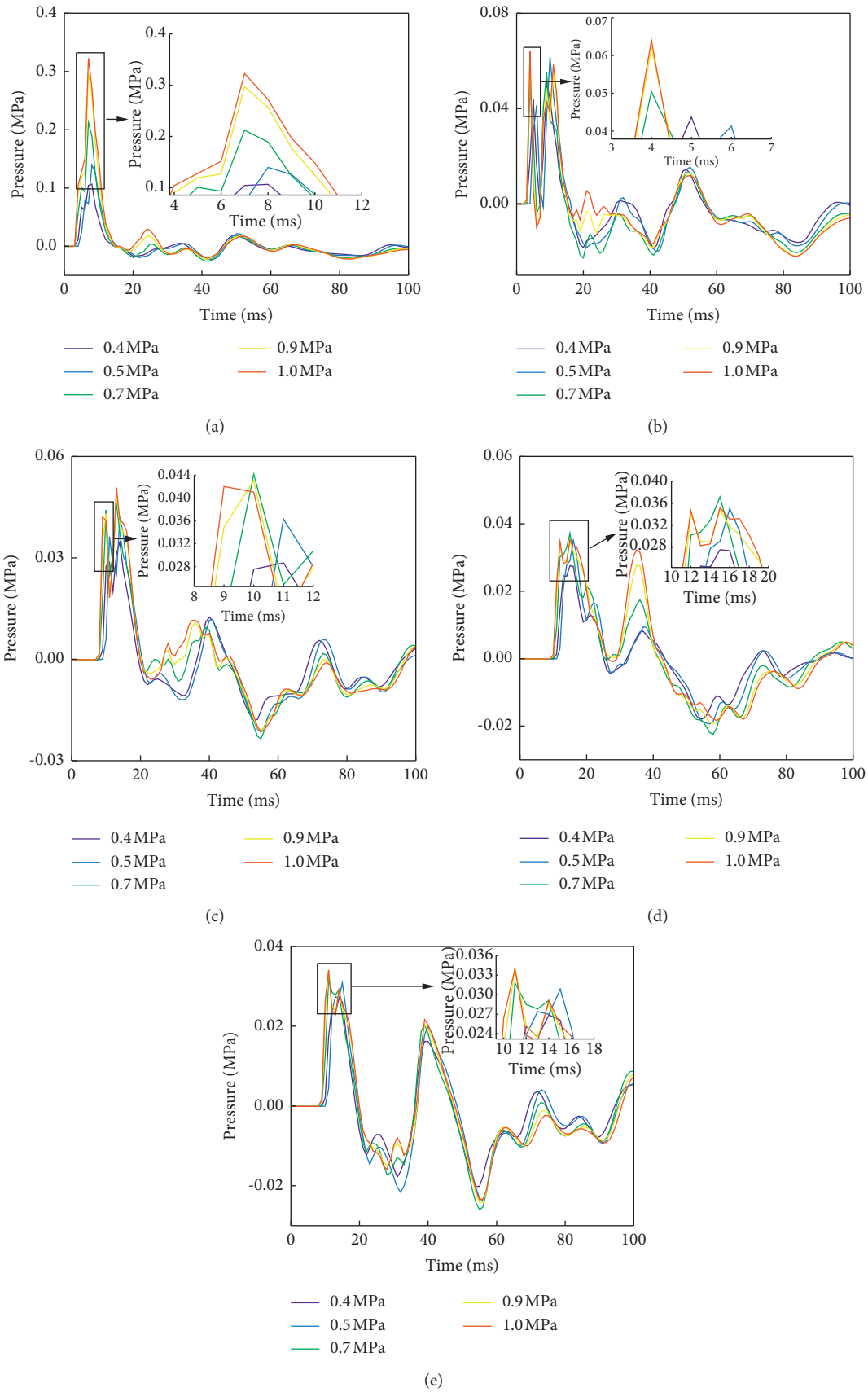
FIGURE 4: Variation of shock wave overpressure with time. (a) Point No. 1. (b) Point No. 2. (c) Point No. 3. (d) Point No. 4. (e) Point No. 5.
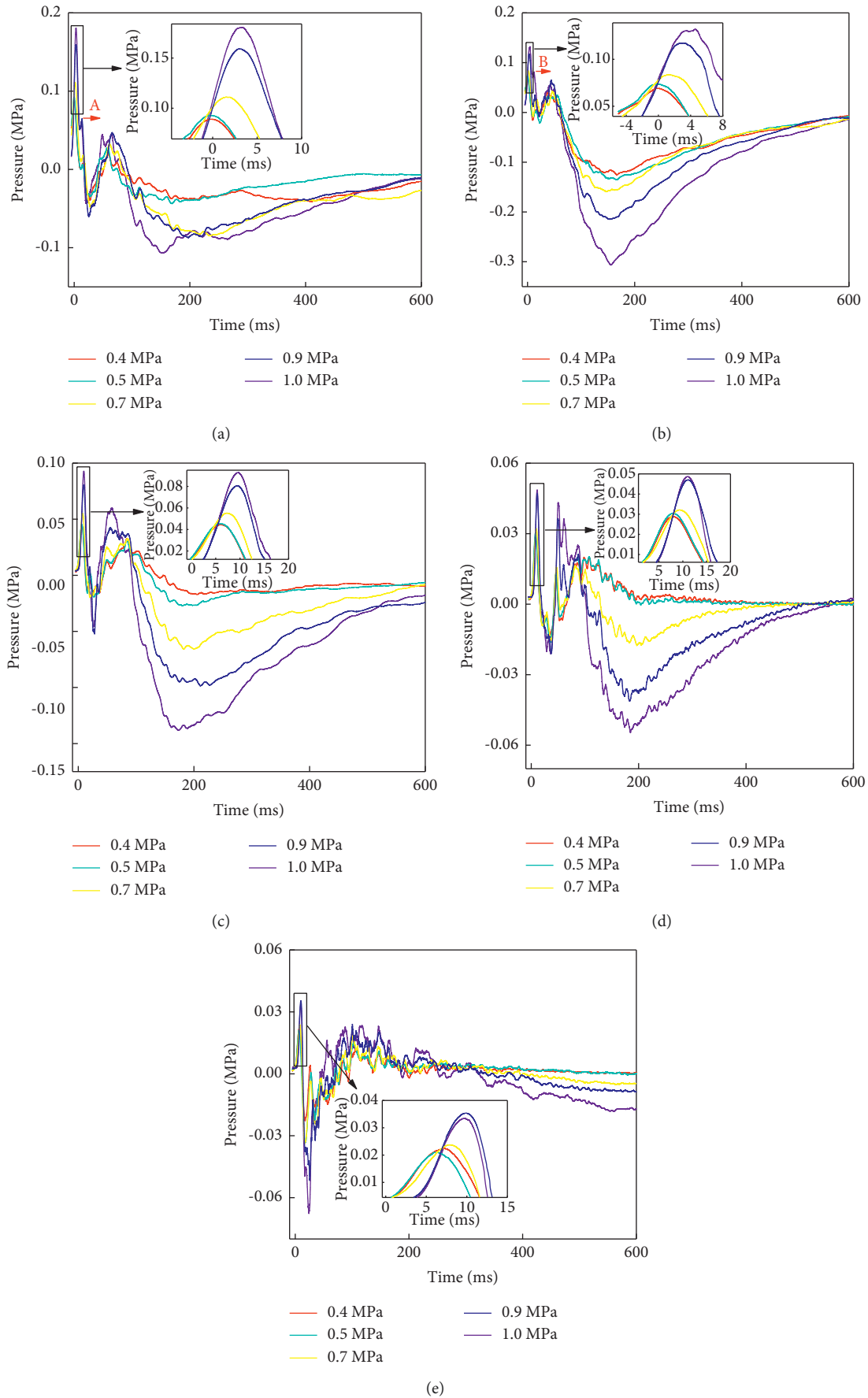
FIGURE 5: Shock wave overpressure change curve (a) Point No. 1. (b) Point No. 2. (c) Point No. 3. (d) Point No. 4. (e) Point No. 5.

Analysis of the simulation results are as follows:

(1) Figure 3(a) shows that at $t = 3$ ms, the shock wave arrives at a corner and diffracts; the shock wave front is spherical, and the maximum impact air velocity on the wave front is approximately 394 m/s. In terms of shock wave velocity, the vector diagram shows that the velocity direction of the shock wave is disordered. The maximum velocity of the disturbed airflow ahead was 56.70 m/s at the corner, and the maximum pressure was at the wall of the straight roadway, which was 0.015 MPa. The impact air pressure of the straight roadway is greater than the impact air pressure at the corner.

(2) Figure 3(b) shows that at $t = 4$ ms, the impact airflow is divided into two parts, and the front end of the impacting airflow propagating in the straight roadway is a positive shock wave; the shock wave propagating along the branch roadway is caused by the impact and reflection on the wall of the roadway. The direction of the impinging airflow is turbulent, and vortex flow is generated at the corner, forming an oblique shock wave. The front velocity of the impinging airflow is approximately 225 m/s in a straight tunnel, and the maximum pressure of the impinging airflow at the corner is approximately 385.17 m/s.

(3) Figure 3(c) shows that at $t = 5$ ms, the shock wave propagating in the straight roadway is reflected by the impact of the damper. Owing to the superposition of the reflected and incident shock waves, the pressure of the shock wave in front of the damper increases, and the maximum pressure is 0.25 MPa. The shock wave propagating in the branch roadway is converted from an oblique shock wave to a positive shock wave. The maximum pressure of the impinging airflow is approximately 146 m/s, and the impinging air velocity is greatly attenuated.

(4) Figure 3(d) shows that at $t = 6$ ms, the impinging airflow along the branch lane propagates to the next corner. Owing to the vortex area, the impinging airflow pressure is unevenly distributed, and the maximum pressure is 0.094 MPa, which is located in the roadway outside the corner. In the airflow disturbance zone in front of the corner, the maximum air velocity is 46.31 m/s. From the impact air velocity vector diagram, it can be found that the direction of the impact air velocity changes after hitting the air door. Owing to the blocking effect of the air door, the impinging air velocity of the airflow in the area near the air door decreases rapidly, and the maximum air velocity is 15 m/s, which is at the edge of the roadway wall.

(5) Figures 3(e) and 3(f) show that as the shock wave continues to propagate forward, the velocity of the impinging airflow decreases owing to the wall friction and the reflection and consumption of the impinging airflow at the corner. At $t = 7$ and 8 ms, the impact of the maximum velocities in the disturbance

zone in front of the airflow are 41.31 and 38.11 m/s, respectively.

(6) Figures 3(g) and 3(h) show that owing to the expansion of the roadway, the shock wave suddenly expands. At this time, the wave front is converted from a plane wave to a spherical shape. Diffraction occurred because of the change in the airflow direction. The airflow pressure and speed are high, and at the corner wall airflow, the pressure and speed are low, resulting in the formation of low-pressure vortices at the corners on both sides. In addition to the shock wave that collides with the facing roadway wall, some shock waves propagate to both sides of the roadway. The maximum pressure of the shock wave propagating in the direction of the wind flow is 0.013 MPa. The maximum pressure of the impinging airflow propagating in the direction opposite to that of the wind flow is 0.011 MPa.

Figure 4 shows the curve of the shock wave overpressure with time. Under various pressure conditions, the following results may be observed from Figure 4:

(1) The maximum overpressure values of the shock waves at measuring points 1, 2, 3, 4, and 5 are 0.32, 0.064, 0.050, 0.035, and 0.034 MPa, respectively, and the maximum overpressure values of measuring points 1 and 3 are caused by the superposition of the reflected wave after the shock wave hits the rigid wall and incident shock wave. Before the impact airflow collides with the roadway wall, the maximum overpressures of the shock waves at measuring points 1 and 3 are 0.104 MPa and 0.042 MPa, respectively. The impact airflow bifurcates; thus, the reflection and wall friction at the corners of the roadway cause the shock wave overpressure to differ when the impinging airflow propagates to the measuring points at various positions. Under the same pressure conditions, the impulsive air pressure tends to attenuate continuously throughout the process, and the smaller the prominent pressure, the smaller the shock wave overpressure.

(2) Comparing the maximum overpressure values of measuring points 1 and 2, the impact of air pressure at measuring point 1 is much greater than that at measuring point 2. This is mainly due to the collision and reflection of the shunt and impact airflow with the corner wall surface, which consumes part of the shock wave. Does energy reduce the shock wave overpressure? Unclear what it means in the bifurcated roadway. Simultaneously, when the impact airflow encounters the bifurcation roadway, the shock wave is diffracted at the corner of the roadway, causing most of the impact airflow to propagate in the straight roadway.

(3) Comparing the maximum overpressure values of measurement at points 2 and 3, the maximum overpressure value of the shock wave at point 2 is greater than that at point 3; however, the pressure

drop is not large. This is due to the maximum overpressure at the two measurement points. The peak appearance time differs from that of the formation mechanism. The maximum pressure peak at point 2 is caused by the incident shock wave passing through the corner, and the appearance time is 4 ms, whereas the maximum pressure monitored by point 3 appears at the second extreme point, at a time of 13 ms. This pressure is caused by the collision of the incident shock wave with the rigid wall facing the T-shaped roadway, and the reflected shock wave generated is superimposed with the incident shock wave, increasing the intensity of the impact airflow in the area.

(4) Comparing the maximum overpressure values of points 4 and 5, the pressure peak at point 5 is slightly smaller than that at point 4. The propagation direction is opposite to the direction of the airflow; therefore, the resistance of the shock wave during the propagation increases, the intensity of the shock wave attenuates, and the shock wave overpressure at point 5 decreases.

(5) Under varying pressure conditions, the greater the outburst pressure, the greater the shock wave overpressure. Simultaneously, owing to the friction of the roadway wall and the obstructive effect of the corners, the shock wave overpressure exhibits a general attenuation trend.

3.2. Analysis of the Experimental Results of the Shock Wave Test System.

Figure 5 shows the change curve of the shock wave overpressure at different time periods. The following results are shown in Figure 5:

(1) The maximum peak overpressure of the shock wave at points 1 and 2 occur at 3.46 and 3.52 ms, respectively. The peak overpressures at the two measuring points are similar in time, indicating that the formation mechanisms most likely are the same and that these are all caused by the incident shock wave. After the maximum pressure peak is monitored at points 1 and 2, the pressure drops rapidly, and the second peak appears. Among these, peak A monitored at point 1, lasted for approximately 13.7 ms and the pressure is 0.064 MPa. Peak B is measured at point 2 and appears at 12.3 ms at 0.08 MPa. It can be seen that the impinging airflow at point 2 at the corner is relatively strong. This is because the impinging airflow collides and is reflected on the roadway wall at the corner. Thus, the reflected shock wave is formed and the subsequent continuous influx of impact leads to an increase in the intensity of the impact airflow at the corners, as shown in Figure 5(a). The peak overpressure of the shock wave monitored at point 1 is greater than that at point 2, which is consistent with the results of the numerical simulations.

(2) The shock wave continues to decay during propagation over a long distance. The maximum shock

Table 3: Model calculation results.

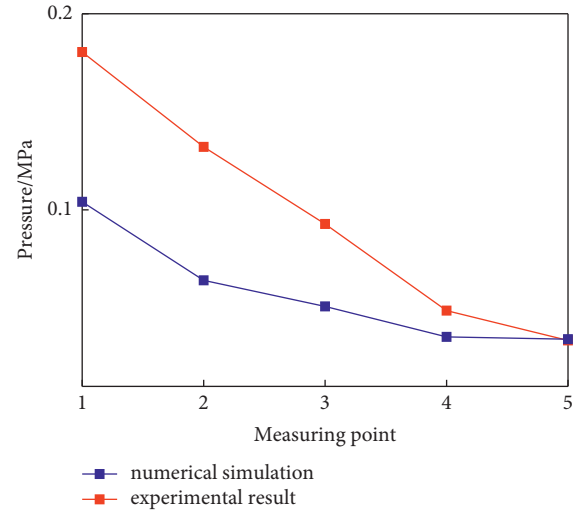| Test pressure/MPa	P_2/kPa	ΔP/kPa
1.0	49	8.5
0.9	47	7.8
0.7	32	6.6
0.5	30	−2.9
0.4	29	−4.1

Figure 6: Comparison of experimental and simulated shock wave overpressures.

wave overpressure monitored at points 3, 4, and 5 are 0.092, 0.048, and 0.035 MPa, respectively. Reflecting shock waves collide with the incident shock waves, further weakening the shock wave energy and causing the shock wave pressure to attenuate; thus, the shock wave pressure at point 3 is reduced. At the same time, the diversion and reflection of the shock wave at the T-shaped roadway (points 4 and 5) causes the shock wave pressure monitored at measuring point 5 to greatly attenuate. Moreover, the shock wave passing through measuring point 5 is subject to frictional resistance and must overcome airflow resistance to propagate forward. This results in a shock wave overpressure at point 5 which is less than that at point 4; this is consistent with the numerical simulation results.

3.3. Analysis of Airflow Reversal in the Fresh Air Tunnel due to Outburst Shock Wave.

The calculation results are listed in Table 3, which shows that, under various outburst pressure conditions, the measured experimental pressure P_2 value is greater than the value calculated using the model. This means that the ventilation resistance in the fresh air roadway is less than the overpressure value of the outburst shock wave, thereby causing the gas to flow backwards. However, the experimental results also revealed another phenomenon. In the near future, without affecting normal ventilation, the corresponding outburst-prevention facilities must be

installed at the connecting lane closest to the fresh air roadway. Similarly, the numerical simulation results are introduced in equation (11). Under all pressure conditions, P_2 is equal to or greater than ΔP, which causes the gas flow to reverse itself. The numerical simulation results are consistent with the calculation results, as shown in Table 3.

Figure 6 shows the comparison between the shock wave measured in the experiment and the shock wave overpressure obtained using numerical simulation. It can be seen that the changing trend of the shock wave overpressure curves obtained from experiment and numerical simulation are consistent, which proves that a reasonably simplified numerical simulation model is feasible.

4. Conclusions

A two-dimensional numerical simulation of propagation of outburst shock wave in the roadway was carried out, was performed in this study. The simulation results show that under identical pressure conditions, the pressure of impinging airflow tends to decay during the entire process, and the lower the protruding pressure, the lower the overpressure of the shock wave. After the shock wave hits the rigid wall, the superposition effect of the reflected wave and incident shock wave was significant. The shock wave was diffracted at the corner of the roadway, causing most of the impact airflow to propagate in the straight roadway.

An outburst shockwave physical simulation experiment was conducted using a new, self-developed coal and gas outburst energy propagation simulation package and parameter determination test device. The experimental results show that the shock wave continued to attenuate after long-distance (over how long?) propagation; it also diffracted at right angles, was weakened, and with its pressure was attenuated (by how much?). The superimposition of the reflected shock wave and the incident shock wave caused peak overpressure of the shock wave in the area to increase per unit area. The experimental results are consistent with the numerical simulation results.

Based on the results of both numerical simulation and physical experiment, combined with a consideration of the relationship between shock wave overpressure and roadway ventilation resistance, it was determined that under various pressure conditions, the measured pressure P_2 value of the experiment was greater than the ventilation resistance. This suggests that the overpressure generated by the prominent shock wave in the fresh air roadway pressure will cause gas backflow. At the same time, this also indicates that when the fresh air roadway is close to the coal uncovering? Position of Shimen, a corresponding antibackflow device should be installed at the location of the connecting road near the fresh air roadway without affecting normal ventilation. These results could be used to improve planning and safety in a variety of mines.

Data Availability

The data used to support the findings of this study have not been made available because they are confidential.

Conflicts of Interest

The authors declare that there are no conflicts of interest regarding the publication of this paper.

Authors' Contributions

In this paper, Xijian Li conceived and designed the experiments. Haiteng Xue and Zhu Liu performed the experiments. Fangrui Dai and Bei Hu processed the data. Haiteng Xue wrote the paper. All authors have read and approved the final manuscript.

Acknowledgments

References

[1] Y. Li and Z. Li, "Forecasting of coal demand in China based on support vector machine optimized by the improved gravitational search algorithm," *Energies*, vol. 12, no. 12, p. 2249, 2019.

[2] Y. Liu, H. Sun, B. Wang, L. Dai, and J. Cao, "Experimental accuracy and stability of gas outburst experimental system," *Geofluids*, vol. 2021, pp. 1–9, Article ID 6678608, 2021.

[3] H. Xie, C. Li, Z. He, C. Li, and F. Gao, "Experimental study on rock mechanical behavior retaining the in situ geological conditions at different depths," *International Journal of Rock Mechanics and Mining Sciences*, vol. 138, Article ID 104548, 2021.

[4] J. Li, H. Xie, L. Chen, C. Li, and Z. He, "Exploring deep-rock mechanics through mechanical analysis of hard-rock in situ coring system," *Advances in Civil Engineering*, vol. 2020, Article ID 8899156, 11 pages, 2020.

[5] H. Xie, M. Gao, R. Zhang, G. W. Peng, and A. Li, "Study on the mechanical properties and mechanical response of coal mining at 1000 m or deeper," *Rock Mechanics and Rock Engineering*, vol. 52, no. 5, pp. 1475–1490, 2019.

[6] F.-h. An, Y.-p. Cheng, L. Wang, and W. Li, "A numerical model for outburst including the effect of adsorbed gas on coal deformation and mechanical properties," *Computers and Geotechnics*, vol. 54, pp. 222–231, 2013.

[7] C. Zhang, E. Wang, J. Xu, and S. Peng, "Research on temperature variation during coal and gas outbursts: implications for outburst prediction in coal mines," *Sensors*, vol. 20, no. 19, p. 5526, 2020.

[8] L. I. Shucai, L. I. Qingchuan, and W. Hanpeng, "Research and development of large-scale true three-dimensional coal and gas outburst quantitative physical simulation test system," *Journal of China Coal Society*, vol. 43, no. S1, pp. 121–129, 2018.

[9] Z. Li, J. Yu, Y. Liu, and M. Zhang, "Numerical analysis of natural gas pressure during coal and gas outbursts," *Energy Science & Engineering*, vol. 9, no. 8, pp. 1068–1079, 2021.

[10] S. Xue, L. Yuan, J. Wang, Y. Wang, and J. Xie, "A coupled DEM and LBM model for simulation of outbursts of coal and gas," *International Journal of Coal Science & Technology*, vol. 2, no. 1, pp. 22–29, 2015.

[11] Y. Tao, J. Xu, D. Liu, and Y. Liang, "Development and validation of THM coupling model of methane-containing coal," *International Journal of Mining Science and Technology*, vol. 22, no. 6, pp. 879–883, 2012.

[12] X. Liu, G. Zhang, Z. Zhang, G. Zhang, and Z. Li, "Application of coupled LDA–KPCA and BO–mkrvm model to predict coal and gas outbursts," *Neural Processing Letters*, vol. 53, no. 4, pp. 2765–2794, 2021.

[13] C. Jianping, D. Jun, and L. Xiangwei, "Research on risk level of coal and gas outburst prediction based on PCA-Fisher discriminant analysis model," *Min Safety & Environmental Protection*, vol. 45, no. 3, pp. 61–71, 2018.

[14] N. Z. Long, A. M. Yi, and X. L. Zhang, "Prediction of coal and gas outburst intensity based on LLE-FOA-BP model," *Industry and Mine Automation*, vol. 45, no. 10, pp. 68–74, 2019.

[15] Y. Yingbiao, Z. Huijuan, and S. Jian, "Prediction of coal and gas outburst based on KPCA and T-S fuzzy neural network," *Measurement Science and Control Technology*, vol. 9, pp. 15–19, 2018.

[16] H. Fu, S. Feng, Z. Gao, and Y. Yang, "Study on double coupling algorithm based model for coal and gas outburst prediction," *China Safety Science Journal*, vol. 28, no. 3, pp. 84–90, 2018.

[17] A. Zhou, K. Wang, L. Fan, and B. Tao, "Propagation characteristics of pulverized coal and gas two-phase flow during an outburst," *PLoS One*, vol. 12, no. 7, Article ID 0180672, 2017.

[18] A. Zhou, K. Wang, and Z. Wu, "Propagation law of shock waves and gas flow in cross roadway caused by coal and gas outburst," *International Journal of Mining Science and Technology*, vol. 24, no. 1, pp. 23–29, 2014.

[19] K. Wang, A. Zhou, J. Zhang, and P. Zhang, "Real-time numerical simulations and experimental research for the propagation characteristics of shock waves and gas flow during coal and gas outburst," *Safety Science*, vol. 50, no. 4, pp. 835–841, 2012.

[20] G. Zhang, *Ventilation safety*, pp. 13–51, China University of Mining and Technology Press, Xuzhou, China, 2011.

[21] X. Li, H. Xue, L. Chen, Z. Liu, F. Dai, and M. Zhang, "Research on energy dissipation law and safety dimensions of protruding shock waves passing through door wall holes," *Journal of China Coal Society*, vol. 46, pp. 1–16, 2021.